

# Resonant Auger decay of $\text{Xe}^* 4d_{5/2}^{-1}6p$ : A contribution to the complete experiment from fluorescence polarization studies

P. O'Keeffe,<sup>1</sup> S. Aloïse,<sup>1,2</sup> S. Fritzsche,<sup>3</sup> B. Lohmann,<sup>4</sup> U. Kleiman,<sup>5,\*</sup> M. Meyer,<sup>1,2</sup> and A. N. Grum-Grzhimailo<sup>1,6</sup>

<sup>1</sup>*LURE, Centre Universitaire Paris—Sud, Bâtiment 209D, F-91898 Orsay Cedex, France*

<sup>2</sup>*CEA/DRECAM/SPAM, CEN Saclay, F-91105 Gif-sur-Yvette, France*

<sup>3</sup>*Fachbereich Physik, Universität Kassel, Heinrich-Plett Strasse 40, D-34132 Kassel, Germany*

<sup>4</sup>*Institut für Theoretische Physik, Westfälische Wilhelms-Universität Münster, Wilhelm-Klemm-Strasse 9, D-48149 Münster, Germany*

<sup>5</sup>*Fritz-Haber-Institut der Max-Planck-Gesellschaft, Faradayweg 4-6, D-14195 Berlin, Germany*

<sup>6</sup>*Institute of Nuclear Physics, Moscow State University, Moscow 119899, Russia*

(Received 5 March 2004; published 12 July 2004)

Fluorescence polarimetry has been used to determine the relative partial-wave Auger decay widths for transitions to states of the  $\text{Xe } 5p^46p$  multiplet after photoexcitation of the  $\text{Xe}^* 4d_{5/2}^{-1}6p(J^*=1)$  resonance by linearly and circularly polarized synchrotron radiation. Combination with data on the angular distribution and spin polarization of the Auger electrons, providing information on the relative phases of the amplitudes, constitutes the complete experiment on the Auger decay. Multiconfiguration relativistic calculations of the amplitudes have been performed and compared to the measurements.

DOI: 10.1103/PhysRevA.70.012705

PACS number(s): 32.80.Hd, 32.80.Fb

## I. INTRODUCTION

Quantum reactions are completely characterized by the absolute magnitudes and phase differences of the complex amplitudes of transitions between the initial state and each of the degenerate final states (channels). Hence the *complete* set of experimental data signifies that from which all of the amplitudes can be extracted. From this information any observable can be predicted, hence providing data for the most comprehensive test of theory [1]. In recent years many experimental investigations of photoelectron and Auger electron emission following inner-shell excitation have been motivated by the quest for such a *complete* experiment. In this paper we focus on the complete experiment for the photoinduced resonant Auger decay: the resonant atomic-core photoexcitation and its subsequent relaxation via the Auger decay [2].

Any experiment can be considered complete only with respect to a model describing the process under investigation. In the case of resonant Auger decay, we imply the two-step model where the direct photoionization is negligible and the amplitude of the resonant process is treated as a product of the excitation and decay amplitudes [3]. Apart from the total intensity, these assumptions make the description of the resonant Auger decay independent of the dipole photoexcitation amplitudes, keeping as the goal of the complete experiment only the determination of the Auger decay amplitudes of the core excited atomic state. In this respect the resonant Auger decay is similar to the normal Auger decay. On the other hand, a single electron emitted after the photoabsorption (in contrast to the two outgoing electrons in the normal Auger decay) makes the analysis of the complete experiment for the resonant Auger decay rather similar to the case of direct photoionization.

Several schemes for feasible experiments yielding information on the Auger decay amplitudes have been discussed theoretically already almost 15 years ago [4]. The main showcase subjects for the complete experiments have been the photoionization and Auger decay of rare-gas atoms. A wide range of experimental techniques have been used to gain information about these processes including high-resolution electron spectroscopy [5–15], fluorescence measurements on the residual ion [16,17], spin-polarization measurements on the emitted electrons [18–26], and measurement of their angular distribution [14,27–31]. Significant progress has been made due to advances associated with the development of third generation synchrotron radiation sources and spin-polarization detection techniques. However, as was demonstrated recently [21,23], a complete set of data, which allows extraction of the amplitudes, cannot be obtained solely from the properties of the emitted photo- or Auger electrons. Generally a combination of different experimental techniques is required to provide the complete information [25,32–34]. Measurements on the residual ion, especially of its alignment and orientation, give access to two additional experimental quantities and can provide the lacking number of independent dynamical parameters. Unlike the parameters of the angular distribution and spin polarization of the outgoing electrons, the ion alignment and orientation are not related to the phase differences between the transition amplitudes and therefore allow extraction of the relative partial cross sections for transitions into different channels. The method of combining data from observations of photo/Auger electrons with the data on the alignment and orientation of the residual ion has been used in Refs. [25,26] for inner-shell photoionization and normal Auger decay processes. For example, in the case of their investigation of the photoionization of Xe from the  $4d$  shell these authors determined the orientation and alignment of the residual ion from the angular distribution and spin-polarization measurements on the subsequent Auger electron.

\*Present address: Department of Physics, Auburn University, 206 Allison Laboratory, Auburn, AL 36849-5311, USA.

In this paper we consider the complete experiment for the resonant Auger decay after photoexcitation with synchrotron radiation (SR) of the strong and well isolated  $\text{Xe}^* 4d_{5/2}^{-1} 6p$  resonance. The validity of the two-step model is well established for this process [11,15,28]. It was also indirectly confirmed theoretically by calculations of the orientation and alignment of the residual ion in the resonant Auger decay of the similar  $3d_{5/2}^{-1} 5p$  state in krypton [35]. The whole process including the subsequent radiative relaxation of the final ionic  $\text{Xe}^{+*} 5p^4 6p$  states can be described as follows:

$$\gamma_{\text{SR}} + \text{Xe} \rightarrow \text{Xe}^* 4d_{5/2}^{-1} 6p (J^* = 1) \quad (1a)$$

$$\hookrightarrow \text{Xe}^{+*} 5p^4 (L_c S_c J_c) 6p [K]_J + e_A^-(\ell j) \quad (1b)$$

$$\hookrightarrow \text{Xe}^{+*} 5p^4 (L'_c S'_c J'_c) 6s, 5d [K']_{J'} + \gamma_{\text{FL}}. \quad (1c)$$

Here Racah notation is used for the  $\text{Xe} \Pi$  ionic levels, while orbital ( $\ell$ ) and total ( $j$ ) angular momenta of the Auger electron  $e_A^-$  characterize different decay channels (corresponding to emission of different partial waves of the Auger electron) for a residual ion with total angular momentum  $J$ . The amplitude of the Auger decay with emission of the  $\varepsilon \ell j$  electron is described by a complex reduced Coulomb matrix element,

$$V_{\ell j} = |V_{\ell j}| \exp i \delta_{\ell j}, \quad (2)$$

where  $|V_{\ell j}|$  is the (non-negative) absolute value of the decay amplitude,  $\delta_{\ell j}$  is its phase, and where the energy of the electron  $\varepsilon$  is omitted for brevity. The relative amplitudes depend only on the absolute ratios  $|V_{\ell j}|/|V_{\ell' j'}|$  and the phase differences  $\delta_{\ell j} - \delta_{\ell' j'}$ . For states with  $J = \frac{1}{2}$  only two amplitudes contribute to the process (1a)—(1b) and in this case only three real parameters have to be determined. In contrast, for the Auger decay to ionic states with  $J > \frac{1}{2}$ , five independent parameters are necessary to completely characterize the Auger decay step within a relativistic approach. These parameters characterize the amplitudes of the three allowed channels and their phase differences. One of the five required parameters, the absolute total Auger width, can be excluded, if we consider relative decay amplitudes instead of their absolute values [36]. For Auger decay from a  $J^* = 1$  initial state, the interdependence of the four relative parameters, which can be found from the measurement of the angular distribution and the spin polarization of the Auger electrons, has been given explicitly in Ref. [37], thereby demonstrating that these methods alone cannot provide the complete information. However, measurements of the alignment and orientation of the discrete ionic  $\text{Xe}^{+*} 5p^4 (L_c S_c J_c) 6p [K]_J$  states after the Auger decay provide additional parameters, which complete the data on the Auger decay step in Eqs. (1a)—(1b). These results can be provided by analysis of the degree of linear and circular polarization of the fluorescence  $\gamma_{\text{FL}}$  induced by linearly and circularly polarized radiation  $\gamma_{\text{SR}}$ , respectively. It should be noted that the resonant Auger decay investigated here differs from previous complete experiments on the Auger decay [22–24,38–40] in that the polarization of the residual ion state needs to be accessed in a different manner, namely by the fluorescence, because this is the only relaxation pathway for the excited ionic states. The fluores-

cence decay channel of the residual ion has been used already for complete characterization of the resonant photoionization of subvalence atomic shells in Ca and Sr [41,42].

The combination of fluorescence measurements with those of measurements on the emitted electron was demonstrated recently for the resonant Auger decay (1a)—(1b) in the special case of decay to an ion with  $J = \frac{1}{2}$  [32]. An ion with  $J = \frac{1}{2}$  can only be oriented and not aligned and so only measurements on the residual ion using circularly polarized excitation and detection analysis provides new information. The absolute ratio of the partial Auger decay amplitudes was extracted in Ref. [32] from the ion orientation parameter and the combination of the fluorescence data with spin polarization [22] and angular distribution [14,31] measurements of the Auger electron for the same process provided the phase shift between the two amplitudes.

In the present paper we extend these results by presenting linear and circular polarization measurements following the Auger decay to substates of the  $\text{Xe} \Pi 5p^4 6p$  multiplet with  $J > \frac{1}{2}$ , thus obtaining experimentally the relative partial widths for these transitions and allowing us to compare them with the theoretical calculations. In comparison with the previous experiments with linearly polarized SR [17], we use a synchrotron radiation source with a higher degree of variable polarization and a higher brilliance allowing us to obtain results of much better quality in terms of their statistical accuracy.

To provide a meaningful analysis of the data we performed a set of relativistic multiconfiguration calculations of the Auger decay amplitudes, extending previous theoretical studies of the resonant Auger decay of the  $\text{Xe}^* 4d_{5/2}^{-1} 6p$  state [15–17,43–49].

The paper is structured as follows. Section II gives a description of the experimental techniques used and summarizes the obtained polarization fluorescence data. Section III describes the procedure of extracting the polarization parameters from these data and presents the deduced values of alignment and orientation of the residual ion. In Sec. IV the relative partial Auger decay widths are determined from these data, while in Sec. V the fluorescence polarization data are combined with those from electron spectroscopy of other authors in order to get further information on the Auger decay amplitudes. In Sec. VI the dynamical models used in the calculations of the decay amplitudes are outlined, followed in Sec. VII by a comparison and discussion of the experimental and theoretical results.

## II. EXPERIMENT

The experiments were carried out at the ELETTRA storage ring in Trieste (Italy) on the “Circular Polarization” beamline. The monochromatized SR provides in the photon energy region around 65 eV an energy resolution of up to 10 meV and a photon flux of about  $10^{12}$  photons/sec in a focal spot of about  $50 \times 50 \mu\text{m}^2$ . For the present experiment the slits of the monochromator were set to  $50 \mu\text{m}$  resulting in a photon energy bandwidth of about 30 meV. An elliptical undulator produces linearly polarized light of high purity

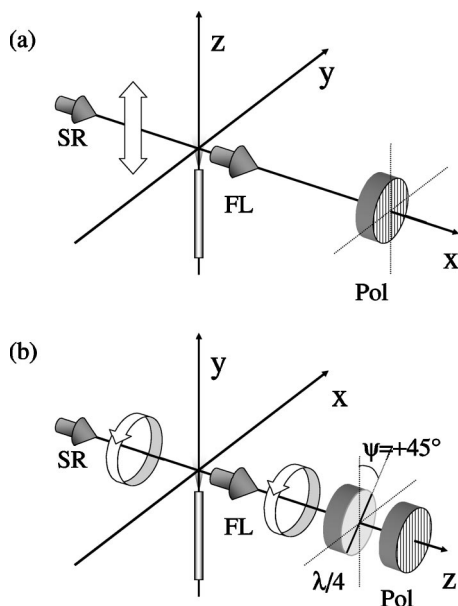


FIG. 1. The geometries used to analyze (a) the degree of linear polarization of the fluorescence (FL) following excitation with linearly polarized SR; (b) the degree of circular polarization of the fluorescence following excitation with circularly polarized SR. Note that different coordinate systems are used in (a) and (b) as the  $z$  axis in (a) is defined by the polarization axis of the SR, while in (b) it is defined by the direction of propagation of the SR.

( $P_L \geq 0.99$ ) and almost pure circular polarization ( $P_C > 0.98$ ).

The experimental setup for measurements of the degree of polarization of the ion fluorescence is similar to that used in previous work [17,32], but is briefly outlined here for clarity. The Xe atoms were flowed into the vacuum chamber via an effusive nozzle of diameter  $300 \mu\text{m}$  to give a background pressure of  $5 \times 10^{-5}$  mbar (background pressure without gas was better than  $1 \times 10^{-7}$  mbar). The fluorescence from the residual ions, which are produced after the resonant Auger decay, is collected and made parallel by a convex lens of 5 cm focal length. The lens assures fluorescence collection within a cone of  $5^\circ$  around the  $z$  axis defined by the direction of propagation of the synchrotron beam. Outside the experimental chamber the fluorescence light was propagated through polarization optics to allow its degree of polarization to be determined. Subsequently, this light was refocused onto the entrance slit of a high-resolution fluorescence spectrometer (Jobin Yvon HR460) for spectral analysis. The resulting wavelength dispersed photons were registered on a liquid-nitrogen-cooled charge-coupled device. The dispersed fluorescence spectra were recorded using a spherical grating of 300 lines/mm giving a spectral resolution  $\Delta\lambda$  of 0.2 nm. With this resolution it was possible to register the entire investigated spectral region (400–600 nm) with a single setting of the grating position. A higher spectral resolution ( $\Delta\lambda = 0.08$  nm) was achieved with an 1800 lines/mm grating and used for an unambiguous assignment of the fluorescence lines.

Analysis of the linear fluorescence polarization was performed after excitation with linearly polarized SR by propa-

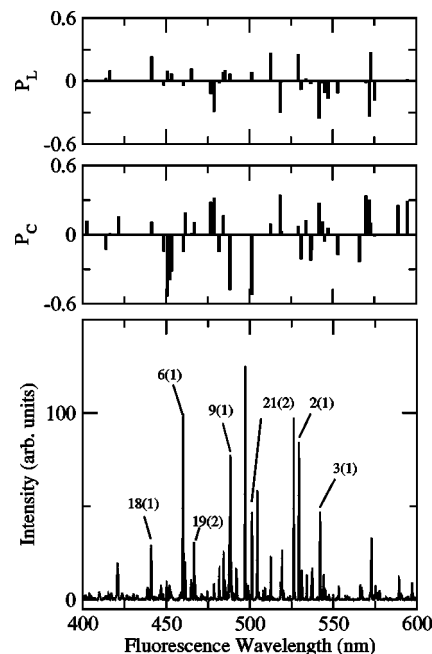


FIG. 2. Dispersed fluorescence spectrum obtained following excitation of the  $\text{Xe}^* 4d_{5/2}^{-1}6p$  resonance (see text). The degree of circular  $P_C$  and linear  $P_L$  polarization for each line is shown in the upper section. A selection of the fluorescence lines is identified using the numerical notation of Table I.

gation through a sheet polarizer (Pol) [see Fig. 1(a)]. The degree of linear polarization  $P_L$  was determined by recording spectral intensities with the axis of the polarizer placed parallel to the electric-field vector of the exciting SR,  $I_{\parallel}$ , and after a rotation of  $90^\circ$  of the polarizer,  $I_{\perp}$ . Application of the following equation then yields  $P_L$ :

$$P_L = \frac{I_{\parallel} - I_{\perp}}{I_{\parallel} + I_{\perp}}. \quad (3)$$

In the case of excitation with circularly polarized SR, analysis of the degree of circular polarization  $P_C$  of the fluorescence was required. For this purpose the geometry was modified by the addition of a rotatable broadband quarter waveplate introduced in front of the sheet polarizer [Fig. 1(b)].  $P_C$  was then determined following excitation with right-handed circularly polarized light (i.e., with helicity +1) by keeping the axis of the linear polarizer parallel to the  $y$  axis and recording the intensities when the fast axis of the quarter waveplate was placed at  $+45^\circ$  ( $I_R$ ) and  $-45^\circ$  ( $I_L$ ) with respect to the  $y$  axis:

$$P_C = \frac{I_R - I_L}{I_R + I_L}. \quad (4)$$

In order to show the overall intensity distribution of the visible fluorescence emitted from the residual  $\text{Xe} \text{ II } 5p^46p$  ions following excitation of the  $\text{Xe}^* 4d_{5/2}^{-1}6p(J^*=1)$  state at  $\gamma_{\text{SR}} = 65.1$  eV, the sum of spectra  $I_{\parallel}$  and  $I_{\perp}$  is displayed in the lowest panel of Fig. 2. The wavelengths of the lines analyzed in this paper are given in Table I where their assignment is given using  $jK$  notation of Ref. [50] and the order of presen-

TABLE I. The degree of circular  $P_C$  and linear  $P_L$  polarization of the fluorescence from the Xe II  $5p^46p$  states produced following excitation of the Xe  $4d_{5/2}^{-1}6p(J^*=1)$  resonance with circularly and linearly polarized synchrotron radiation, respectively. The corresponding values of orientation  $\mathcal{A}_{10}^C$  and alignment  $\mathcal{A}_{20}^L$  parameters of the ionic states produced following the Auger decay are given (see text).

No.	Fluorescence transition		$\lambda$ (fluo)	$P_C$	$P_L$	$\mathcal{A}_{10}^C$	$\mathcal{A}_{20}^L$
	Initial state	Final state					
1	$(^3P_2)6p[2]_{3/2}$	$(^3P_2)6s[2]_{5/2}$	533.933	<b>+0.121(20)</b>	<b>+0.017(15)</b>	-0.39(14)	-0.29(27)
2	$(^3P_2)6p[2]_{5/2}$	$(^3P_2)6s[2]_{5/2}$	529.222	<b>+0.071(12)</b>	<b>+0.255(10)</b>	+0.32(6)	+0.78(9)
		$(^3P_2)5d[2]_{5/2}$	603.620	+0.079(54)	+0.270(40)		
		$(^3P_2)5d[3]_{7/2}$	605.115	-0.116(51)	-0.092(20)		
3	$(^3P_2)6p[3]_{5/2}$	$(^3P_2)6s[2]_{3/2}$	541.915	<b>+0.275(15)</b>	<b>-0.354(12)</b>	+0.46(9)	+0.88(16)
		$(^3P_2)5d[3]_{7/2}$	553.107	-0.174(22)	-0.113(20)		
		$(^3P_2)5d[2]_{3/2}$	571.961	+0.300(18)	-0.337(31)		
4	$(^3P_2)6p[1]_{1/2}$	$(^3P_2)6s[2]_{3/2}$	537.239	<b>-0.133(11)</b>	<b>+0.009(30)</b>	+0.44(3)	
		$(^3P_2)5d[1]_{1/2}$	594.553	+0.292(92)	+0.015(80)		
5	$(^3P_2)6p[3]_{7/2}$	$(^3P_2)6s[2]_{5/2}$	484.433	<b>+0.166(8)</b>	<b>+0.082(25)</b>	+0.31(9)	-0.36(15)
		$(^3P_2)5d[3]_{7/2}$	547.261	+0.057(61)	-0.168(73)		
6	$(^3P_2)6p[1]_{3/2}$	$(^3P_2)6s[2]_{3/2}$	460.303	<b>-0.146(12)</b>	<b>-0.040(5)</b>	-0.40(3)	-0.09(1)
		$(^3P_2)5d[2]_{3/2}$	481.802	-0.147(15)	-0.019(40)		
7	$(^3P_0)6p[1]_{1/2}$	$(^3P_0)6s[0]_{1/2}$	519.137	<b>+0.027(15)</b>	<b>-0.010(12)</b>	+0.05(3)	
8	$(^3P_1)6p[0]_{1/2}$	$(^3P_1)6s[1]_{3/2}$	543.896	<b>+0.113(18)</b>	<b>-0.018(20)</b>	-0.32(5)	
9	$(^3P_0)6p[1]_{3/2}$	$(^3P_0)6s[0]_{1/2}$	488.353	<b>-0.480(15)</b>	<b>+0.068(12)</b>	-0.54(2)	-0.14(3)
		$(^3P_1)6[1]_{3/2}$	530.927	-0.210(10)	-0.082(18)		
11	$(^3P_1)6p[2]_{3/2}$	$(^3P_0)6s[0]_{1/2}$	452.421	<b>-0.388(25)</b>	<b>+0.013(57)</b>	-0.42(3)	-0.02(11)
12	$(^3P_1)6p[1]_{3/2}$	$(^3P_1)6s[1]_{3/2}$	465.194	+0.009(15)	+0.115(32)	-0.02(2)	+0.32(4)
		$(^3P_2)5d[0]_{1/2}$	545.045	-0.058(20)	-0.108(24)		
		$(^3P_1)6s[1]_{1/2}$	575.103	<b>-0.014(16)</b>	<b>-0.183(21)</b>		
13	$(^3P_1)6p[1]_{1/2}$	$(^3P_2)5d[0]_{1/2}$	536.807	-0.223(35)	-0.024(40)	-0.33(3)	
		$(^3P_1)6s[1]_{1/2}$	565.938	<b>-0.235(18)</b>	<b>-0.002(40)</b>		
14	$(^1D_2)6p[3]_{5/2}$	$(^3P_1)5d[1]_{3/2}$	476.905	<b>+0.282(138)</b>	<b>-0.120(145)</b>	+0.62(44)	+0.49(62)
		$(^3P_1)5d[2]_{3/2}$	569.961	+0.335(185)	-0.018(110)		
15	$(^1D_2)6p[1]_{3/2}$	$(^3P_2)5d[0]_{1/2}$	421.469	+0.153(21)	-0.004(15)	-0.33(3)	-0.05(22)
		$(^3P_0)5d[2]_{3/2}$	448.595	-0.145(61)	-0.041(54)		
		$(^3P_0)5d[2]_{5/2}$	461.550	<b>+0.189(20)</b>	<b>+0.005(24)</b>		
		$(^3P_1)5d[2]_{5/2}$	589.329	+0.255(50)	-0.008(17)		
16	$(^1D_2)6p[3]_{7/2}$	$(^3P_0)5d[2]_{5/2}$	453.249	<b>-0.319(45)</b>	<b>+0.070(41)</b>	-0.40(8)	-0.20(13)
17	$(^1D_2)6p[2]_{3/2}$	$(^3P_1)5d[1]_{3/2}$	416.216	+0.008(43)	+0.097(64)	+0.01(5)	+0.23(8)
		$(^3P_1)5d[2]_{3/2}$	485.377	<b>+0.003(20)</b>	<b>+0.100(34)</b>		
18	$(^1D_2)6p[2]_{5/2}$	$(^1D_2)6s[2]_{5/2}$	441.484	<b>+0.109(10)</b>	<b>+0.233(30)</b>	+0.35(3)	+0.49(7)
		$(^3P_1)5d[2]_{3/2}$	478.777	+0.320(30)	-0.290(38)		
		$(^3P_1)5d[2]_{5/2}$	512.570	+0.092(19)	+0.265(18)		
		$(^1D_2)6s[2]_{3/2}$	518.448	+0.341(25)	-0.297(38)		
		$(^3P_1)5d[3]_{5/2}$	572.691	+0.100(30)	+0.272(26)		
19	$(^1D_2)6p[1]_{1/2}$	$(^3P_1)5d[1]_{3/2}$	402.519	+0.118(64)	+0.010(67)	-0.29(5)	
		$(^3P_1)5d[2]_{3/2}$	466.849	<b>+0.107(16)</b>	<b>-0.005(28)</b>		
20	$(^1S_0)6p[1]_{1/2}$	$(^1D_2)5d[1]_{3/2}$	413.881	<b>-0.130(150)</b>	<b>+0.024(73)</b>	+0.47(54)	
21	$(^1S_0)6p[1]_{3/2}$	$(^1D_2)5d[1]_{1/2}$	450.711	-0.534(20)	+0.094(22)	-0.53(2)	-0.15(2)
		$(^1S_0)6s[0]_{1/2}$	501.283	<b>-0.522(15)</b>	<b>+0.081(8)</b>		



tation of the Xe II  $5p^46p$  states follows previous publications [17,31]. Only lines which are well resolved were analyzed for polarization dependence and therefore not all lines shown in the spectrum are tabulated in Table I. A selection of lines presented in Table I is identified in Fig. 2 using the numerical notation shown in the first column of Table I to identify the initial state and the number in parentheses indicates the final state. For example, the fluorescence line at 460.303 nm is given the numerical designation 6(1), where 6 refers to the initial state of the fluorescence,  $5p^4(^3P_2)6p[1]_{3/2}$ , and (1) refers to the final state,  $5p^4(^3P_2)6s[2]_{3/2}$ , in the order presented in Table I. The identification of the other observed lines can be obtained with the help of Table II in Ref. [17], where the relative intensities are given for each transition. For the assignment of the individual fluorescence lines, the high-resolution spectra were used in combination with the tables of spectral lines for Xe II [50] and Xe III [51].

The results of our linear and circular polarization analysis to determine the values of  $P_L$  and  $P_C$  are visualized as a histogram in the upper part of Fig. 2 and the numerical values are listed in Table I. The final spectrum for each polarization setting used in the above analysis is the sum of eight individual spectra and the errors given in Table I were calculated including statistical and systematic errors.

Numerous checks were performed to ensure self-consistency of the data. For determining the degree of linear polarization, for instance, a convenient internal calibration of the data exists in that fluorescence lines from Xe II  $5p^46p$  states with  $J=\frac{1}{2}$  cannot be aligned and hence show a vanishing linear polarization. Fluorescence transitions originating from  $J=\frac{1}{2}$  states are distributed throughout the spectral region of interest. To remove any possible wavelength or polarization dependence of the detection system the intensities of the spectra were normalized such that each of these lines showed zero polarization. This correction leads to a maximal change of the intensities of the order of only 5%. The consistency of the circular polarization data was also verified by measuring the degree of polarization using three separate methods: changing the helicity of the SR, rotating the sheet polarizer by  $90^\circ$  and rotating the quarter waveplate by  $90^\circ$ . Each of these methods gave similar results and the resulting errors quoted in Table I are calculated from the standard deviation of these values.

### III. ORIENTATION AND ALIGNMENT OF THE IONIC STATES

The next step of the analysis is to deduce, from the above fluorescence polarization data, the orientation  $\mathcal{A}_{10}(J)$  and alignment  $\mathcal{A}_{20}(J)$  transferred to the Xe II  $5p^46p$  states during the Auger process. As can be seen from Table I, the values of  $P_C$  and  $P_L$  measured for transitions from the same Xe II  $5p^46p$  state to different final states differ in magnitude and even in sign. This is due to the fact that the degree of polarization is also dependent on the total angular momentum of the final state of the radiative transition  $J'$ . Another factor, which needs to be taken into account when extracting orientation and alignment from the polarization data, is the depolarization of the initial Xe II  $5p^46p$  states before fluorescence

takes place. These points are illustrated by the equations connecting  $P_C$  and  $P_L$  to  $\mathcal{A}_{10}$  and  $\mathcal{A}_{20}$  [52]:

$$P_C = \frac{\sqrt{3}\alpha_1^{\gamma}\bar{\mathcal{A}}_{10}^C}{\alpha_2^{\gamma}\bar{\mathcal{A}}_{20}^C + 1}, \quad (5)$$

$$P_L = \frac{3\alpha_2^{\gamma}\bar{\mathcal{A}}_{20}^L}{\alpha_2^{\gamma}\bar{\mathcal{A}}_{20}^L - 2}, \quad (6)$$

where  $\alpha_k^{\gamma}$  are known intrinsic anisotropy parameters for the emitted radiation, which depend only on the angular momenta of the initial ( $J$ ) and final ( $J'$ ) ionic states in the radiative transition:

$$\alpha_k^{\gamma}(J, J') = \sqrt{\frac{3}{2}}\hat{J}(-1)^{J+J'+k+1} \begin{Bmatrix} 1 & 1 & k \\ J & J & J' \end{Bmatrix}. \quad (7)$$

Here and below we abbreviate  $\hat{a} = \sqrt{2a+1}$  and use the standard notations for the  $nj$  symbols. In Eqs. (5) and (6) the quantities  $\bar{\mathcal{A}}_{k0}^C$  and  $\bar{\mathcal{A}}_{k0}^L$  ( $k=1, 2$ ) are the statistical tensors of the Xe II state at the moment of radiative decay, produced by circularly ( $C$ ) and linearly ( $L$ ) polarized SR. It is implied that  $\bar{\mathcal{A}}_{k0}^C(J)$  and  $\bar{\mathcal{A}}_{k0}^L(J)$  are taken in the coordinate systems with the quantization axis along the SR beam and along the electric field vector of the SR beam, respectively. The quantities  $\bar{\mathcal{A}}_{k0}^{C,L}(J)$  are related to the initial statistical tensors after the Auger decay via the depolarization factors  $D_k(J)$ :

$$\bar{\mathcal{A}}_{k0}^{C,L}(J) = D_k(J)\mathcal{A}_{k0}^{C,L}(J). \quad (8)$$

The factors  $D_k(J)$  are treated within the isotropic model of the radiation cascade, which has been justified in our case [17]. They can be presented in a product form,  $D_k(J) = D(J)G_k(J)$ , with the factor  $D(J)$  due to the cascade depolarization and the factors  $G_k(J)$  due to depolarization caused by hyperfine interactions. The cascading depolarization factors  $D(J)$  have been presented in Ref. [17] for all the Xe II  $5p^46p$  states with  $J > \frac{1}{2}$ . The depolarization factors  $D(J)$  for the  $J=\frac{1}{2}$  states 4, 7, 8, 13, 19, and 20 have been derived in a similar way and take the values 0.81(8), 0.78(18), 0.95(4), 0.97(3), 0.99(1), 0.75(4), respectively. The factors  $G_k(J)$  are calculated similar to Ref. [17] by making use of the assumption of well isolated hyperfine structure levels according to

$$G_k(J) = \hat{I}^{-2} \sum_F \hat{F}^4 \begin{Bmatrix} F & F & k \\ J & J & I \end{Bmatrix}^2, \quad (9)$$

where the summation over  $F$  runs over all possible values of the total angular momentum  $\vec{F} = \vec{J} + \vec{I}$  with  $\vec{I}$  being the nuclear spin. In order to find the final results for  $G_k(J)$  the subsequent weighting according to the abundances of the Xe isotopes was done. This procedure leads to the values  $G_1(\frac{1}{2}) = 0.74$ ,  $G_1(\frac{3}{2}) = 0.86$ ,  $G_1(\frac{5}{2}) = 0.93$ ,  $G_1(\frac{7}{2}) = 0.96$ ,  $G_2(\frac{3}{2}) = 0.75$ ,  $G_2(\frac{5}{2}) = 0.83$ ,  $G_2(\frac{7}{2}) = 0.89$ .

Values of the orientation and alignment parameters, extracted from the measured values of  $P_L$  and  $P_C$  are presented for all the final ionic states in the last columns of Table I.

Although the values of  $\mathcal{A}_{10}^C$  and  $\mathcal{A}_{20}^L$  extracted from different fluorescence lines, but originating from the same ionic state, are consistent, the values presented in Table I were obtained from the data, marked by the bold-type characters. Similar to Ref. [17], the criteria have been the intensity of the lines and the possibility to separate them completely from other close-lying transitions.

#### IV. EVALUATION OF RELATIVE PARTIAL DECAY WIDTHS

As the first application of our data, we deduce the relative partial decay widths  $\Gamma_{\ell j}/\Gamma$  for Auger transitions from the  $\text{Xe}^* 4d_{5/2}6p(J^*=1)$  state to the  $\text{Xe} \Pi 5p^46p$  manifold. Within the two-step model of the Auger process the alignment and orientation parameters of the residual ion produced after the Auger decay take the form [52,53]

$$\mathcal{A}_{k0}(J) = \mathcal{A}_{k0}(J^*=1) \sqrt{3} \hat{J} \sum_{\ell j} (-1)^x \begin{Bmatrix} 1 & 1 & k \\ J & J & j \end{Bmatrix} \frac{\Gamma_{\ell j}}{\Gamma}. \quad (10)$$

In this expression  $\chi = J + j + k + 1$  and we introduced the partial decay width  $\Gamma_{\ell j} = 2\pi |V_{\ell j}|^2$  for emission of the Auger electron into the  $\varepsilon \ell j$  continuum and the total width  $\Gamma = \sum_{\ell j} \Gamma_{\ell j}$ . Equation (10) describes a polarization transfer to a residual ion from an Auger state with unit total angular momentum initially characterized by the orientation  $\mathcal{A}_{10}(J^*=1) = \sqrt{3}/2$  (for SR with helicity = +1) and/or the alignment  $\mathcal{A}_{20}(J^*=1) = -\sqrt{2}$  (for linearly polarized SR). The residual ion parameters (10) depend only on the relative partial widths  $\Gamma_{\ell j}$ . These  $\Gamma_{\ell j}$  were extracted from the present data  $\mathcal{A}_{10}(J)$  and  $\mathcal{A}_{20}(J)$  given in Table I by applying Eq. (10) and are collected in Tables II–V together with the results of theoretical calculations. The numerical designation given in column 1 corresponds to the labeling given in Table I; to facilitate comparison with the Auger electron analysis [15] the numbering of the corresponding electron lines are also given in parentheses. For clarity the expanded versions of Eq. (10) for the particular transitions considered in this paper are shown in the Appendix [see Eqs. (A2), (A5), (A9), and (A13)]. The error bars for the relative widths were determined by propagation of the errors in the polarizations  $P_L$ ,  $P_C$ , and in the depolarization factors  $D(J)$ . The results for the relative partial widths (branching ratios) will be discussed in Sec. VII.

To visualize the polarization transfer during the Auger decay and its connection to the partial widths, we present as an example a graphical illustration of the angular momentum distributions for the decay to the  $(^3P_2)6p[3]_{7/2}$  state (no. 5, see Table V) following excitation with circularly polarized light. In the case of excitation with right-handed circularly polarized light only the angular momentum substate with  $M_{J^*} = +1$  is populated in the  $(J^*=1)$  initial state. The subsequent Auger decay to an ion with  $J = \frac{7}{2}$  involves emission of  $\varepsilon d_{5/2}$ ,  $\varepsilon g_{7/2}$ , and  $\varepsilon g_{9/2}$  partial waves, which give distinctly different polarization distributions of the residual ion. This is shown in Fig. 3, which was produced using a semiclassical description of the angular momentum vector distribution [54],

TABLE II. Relative partial widths  $\Gamma_{\ell j}/\Gamma$  of the Auger decay into the  $\text{Xe} \Pi 5p^46p$  states with  $J = \frac{1}{2}$  and relative phases of the amplitudes  $\delta_{\ell j} - \delta_{\ell' j'}$ . First line, present experiment; second line, present theory, model (e); third line, theory of Lagutin *et al.* [16]. In addition to the  $jK$  notation, the corresponding  $LS$ -coupling notation and numerical designation (given in parentheses in column 1) of Aksela *et al.* [15] are also given for the final states of the Auger decay.

No.	Final state	$\Gamma_{\ell j}/\Gamma$ (%)		$\delta_1^a$
		$s_{1/2}$	$d_{3/2}$	
4	$(^3P_2)6p[1]_{1/2}$	63(7)	37(7)	
(23)	$(^3P)6p^2S_{1/2}$	44.1	55.9	−2.185
		30.1	69.9	
7	$(^3P_0)6p[1]_{1/2}$	36(4)	64(4)	
(28)	$(^3P)6p^2P_{1/2}$	0.0	100.0	−2.208
		0.0	100.0	
8	$(^3P_1)6p[0]_{1/2}$	12(7)	88(7)	
(30)	$(^3P)6p^4P_{1/2}$	6.3	93.7	−2.195
		6.9	93.1	
13	$(^3P_1)6p[1]_{1/2}$	12(4)	88(4)	
(36)	$(^3P)6p^4D_{1/2}$	1.2	98.8	−2.211
		1.4	98.6	
19	$(^1D_2)6p[1]_{1/2}$	14(6)	86(6)	
(46)	$(^1D)6p^2P_{1/2}$	11.0	89.0	0.885
		15.6	84.4	
20	$(^1S_0)6p[1]_{1/2}$	65(63)	35(63)	
(65)	$(^1S)6p^2P_{1/2}$	70.4	29.6	0.795
		8.3	91.7	

$$^a \delta_1 = \delta_{s_{1/2}} - \delta_{d_{3/2}}.$$

$$W(\theta) = \hat{J}^{-1} \sum_{k=0}^2 \frac{\hat{k}}{\sqrt{4\pi}} \mathcal{A}_{k0}(J) P_k(\cos \theta), \quad (11)$$

where  $\theta$  is the angle between the angular momentum vector and the quantization axis and  $P_k(x)$  are the Legendre polynomials. Adding these distributions with coefficients given by the partial widths into each channel (given in Table V) results in the angular momentum distribution, which governs the fluorescence polarization. In the particular case illustrated in Fig. 3 it can be seen that the Auger decay is dominated by emission of the  $\varepsilon d_{5/2}$  wave, which results in a positive orientation of the angular momentum distribution of the ion. Hence the angular momentum of the ion with all decay channels taken into account also shows a positive orientation (positive  $M_J$  states are preferentially populated) as can be seen by the positive value of  $\mathcal{A}_{10}^C$  for this state (no. 5 in Table I).

#### V. COMBINATION OF FLUORESCENCE AND ELECTRON SPECTROSCOPIC DATA

To gain information about the phase differences of the Auger decay amplitudes (2) the fluorescence polarization data need to be combined with measurements on the angular distribution and spin polarization of the Auger electron, de-

TABLE III. Same as Table II, but for final states with  $J=\frac{3}{2}$ .

No.	Final state	$\Gamma_{\ell j}/\Gamma$ [%]			$\delta_1^a$	$\delta_2^b$
		$s_{1/2}$	$d_{3/2}$	$d_{5/2}$		
1	( <sup>3</sup> P <sub>2</sub> )6p[2] <sub>3/2</sub>	14(13)	2(21)	84(20)		
(19)	( <sup>3</sup> P)6p <sup>4</sup> P <sub>3/2</sub>	0.2	1.4	98.4	-2.235	-0.090
		0.3	1.2	98.5		
6	( <sup>3</sup> P <sub>2</sub> )6p[1] <sub>3/2</sub>	6(3)	16(3)	78(5)		
(26)	( <sup>3</sup> P)6p <sup>2</sup> P <sub>3/2</sub>	0.3	19.3	80.4	-2.277	-0.096
		0.2	15.5	84.3		
9	( <sup>3</sup> P <sub>0</sub> )6p[1] <sub>3/2</sub>	1(2)	7(2)	92(3)		
(31)	( <sup>3</sup> P)6p <sup>2</sup> D <sub>3/2</sub>	0.0	0.9	99.1	-2.249	3.083
		0.0	0.4	99.6		
11	( <sup>3</sup> P <sub>1</sub> )6p[2] <sub>3/2</sub>	2(6)	19(7)	79(4)		
(33)	( <sup>3</sup> P)6p <sup>4</sup> S <sub>3/2</sub>	0.1	8.1	91.8	0.886	-0.066
		0.1	8.1	91.8		
12	( <sup>3</sup> P <sub>1</sub> )6p[1] <sub>3/2</sub>	2(2)	55(3)	43(3)		
(34)	( <sup>3</sup> P)6p <sup>4</sup> D <sub>3/2</sub>	0.1	65.4	34.5	-2.227	3.103
		0.1	56.2	43.8		
15	( <sup>1</sup> D <sub>2</sub> )6p[1] <sub>3/2</sub>	5(10)	19(15)	76(7)		
(41)	( <sup>1</sup> D)6p <sup>2</sup> P <sub>3/2</sub>	1.1	19.9	79.0	-2.291	3.075
		1.9	18.3	79.8		
17	( <sup>1</sup> D <sub>2</sub> )6p[2] <sub>3/2</sub>	7(5)	49(7)	44(7)		
(43)	( <sup>1</sup> D)6p <sup>2</sup> D <sub>3/2</sub>	1.7	46.2	52.1	-2.288	3.088
		3.3	55.4	41.3		
21	( <sup>1</sup> S <sub>0</sub> )6p[1] <sub>3/2</sub>	2(2)	6(2)	92(2)		
(67/68)	( <sup>1</sup> S)6p <sup>2</sup> P <sub>3/2</sub>	0.0	0.4	99.6	0.792	-0.018
		0.0	0.2	99.8		

$$^a\delta_1 = \delta_{s_{1/2}} - \delta_{d_{5/2}}.$$

$$^b\delta_2 = \delta_{d_{3/2}} - \delta_{d_{5/2}}.$$

scribed in our case by four intrinsic parameters, for example,  $\alpha_2, \xi_2, \beta_1$ , and  $\gamma_1$  [52,55–57]. The parameters  $\beta_1$  and  $\gamma_1$  describe the spin polarization of the Auger electron due to polarization transfer. However, the parameters presently available in the literature from experiments on electron spectroscopy following the resonance Auger decay of the Xe 4d<sub>5/2</sub><sup>-1</sup>6p( $J^*=1$ ) state are  $\alpha_2$  and  $\xi_2$ :

(i) The anisotropy parameter  $\alpha_2$  describes the angular distribution of Auger electrons [58]

$$I(\vartheta) = \frac{I_0}{4\pi} [1 + \alpha_2 \mathcal{A}_{20} P_2(\cos \vartheta)], \quad (12)$$

where  $\vartheta$  is the angle between the directions of Auger electron emission and the quantization axis,  $I_0$  denotes the total intensity of the Auger decay, and  $\mathcal{A}_{20} = \mathcal{A}_{20}(J^*=1)$ . The anisotropy parameter is expressed in the general form as

$$\alpha_2 = \sqrt{3}(-1)^{J+1/2} \sum_{\ell\ell'jj'} \hat{\ell} \hat{\ell}' \hat{j} \hat{j}' (\ell 0, \ell' 0 | 20) \begin{Bmatrix} 1 & 1 & 2 \\ j & j' & J \end{Bmatrix} \times \begin{Bmatrix} \ell & \ell' & 2 \\ j' & j & \frac{1}{2} \end{Bmatrix} \frac{2\pi}{\Gamma} V_{\ell j} V_{\ell' j'}^*, \quad (13)$$

where  $(j_1 m_1, j_2 m_2 | j_3 m_3)$  is the Clebsch-Gordan coefficient.

 TABLE IV. Same as Table II, but for final states with  $J=\frac{5}{2}$ .

No.	Final state	$\Gamma_{\ell j}/\Gamma$ [%]			$\delta_1^a$	$\delta_2^b$
		$d_{3/2}$	$d_{5/2}$	$g_{7/2}$		
2	( <sup>3</sup> P <sub>2</sub> )6p[2] <sub>5/2</sub>	19(2)	79(8)	2(9)		
(20)	( <sup>3</sup> P)6p <sup>4</sup> P <sub>5/2</sub>	3.3	95.9	0.8	-2.814	-0.079
		3.2	96.0	0.8		
3	( <sup>3</sup> P <sub>2</sub> )6p[3] <sub>5/2</sub>	1(3)	103(15)	-4(15)		
(22)	( <sup>3</sup> P)6p <sup>2</sup> D <sub>5/2</sub>	2.2	96.6	1.1	-2.811	-0.085
		2.3	96.6	1.2		
10	( <sup>3</sup> P <sub>1</sub> )6p[2] <sub>5/2</sub>					
(32)	( <sup>3</sup> P)6p <sup>4</sup> D <sub>5/2</sub>	41.0	52.1	6.9	-2.723	-0.103
		40.9	57.0	2.1		
14	( <sup>1</sup> D <sub>2</sub> )6p[3] <sub>5/2</sub>	27(35)	79(52)	6(60)		
(39)	( <sup>1</sup> D)6p <sup>2</sup> F <sub>5/2</sub>	16.4	72.9	10.7	-2.659	3.101
		19.1	64.6	16.3		
18	( <sup>1</sup> D <sub>2</sub> )6p[2] <sub>5/2</sub>	22(5)	77(5)	1(5)		
(44)	( <sup>1</sup> D)6p <sup>2</sup> D <sub>5/2</sub>	12.7	77.1	10.2	-2.627	3.109
		12.9	73.1	14.0		

$$^a\delta_1 = \delta_{g_{7/2}} - \delta_{d_{5/2}}.$$

$$^b\delta_2 = \delta_{d_{3/2}} - \delta_{d_{5/2}}.$$

(ii) The dynamical spin-polarization parameter  $\xi_2$  describes the spin component of the Auger electrons following excitation with linearly polarized radiation [55,59],

$$P_y = \frac{\xi_2 \mathcal{A}_{20} \sin 2\vartheta}{1 + \alpha_2 \mathcal{A}_{20} P_2(\cos \vartheta)}, \quad (14)$$

where the notation used is the same as in Eq. (12) and

$$\xi_2 = -3\sqrt{15} \sum_{\ell j \leq \ell' j'} (-1)^{\ell-J-j'-1} \hat{\ell} \hat{\ell}' \hat{j} \hat{j}' (\ell 0, \ell' 0 | 20)$$

$$\times \begin{Bmatrix} 1 & 1 & 2 \\ j & j' & J \end{Bmatrix} \begin{Bmatrix} \ell & \frac{1}{2} & j \\ \ell' & \frac{1}{2} & j' \\ 2 & 1 & 2 \end{Bmatrix} \frac{2\pi}{\Gamma} \text{Im}(V_{\ell j} V_{\ell' j'}^*). \quad (15)$$

Explicit expressions for the parameters (13) and (15) in the

 TABLE V. Same as Table II, but for final states with  $J=\frac{7}{2}$ .

No.	Final state	$\Gamma_{\ell j}/\Gamma$ [%]			$\delta_1^a$	$\delta_2^b$
		$d_{5/2}$	$g_{7/2}$	$g_{9/2}$		
5	( <sup>3</sup> P <sub>2</sub> )6p[3] <sub>7/2</sub>	57(12)	12(10)	31(8)		
(24)	( <sup>3</sup> P)6p <sup>4</sup> D <sub>7/2</sub>	28.9	1.8	69.3	-0.377	3.104
		25.4	1.5	73.1		
16	( <sup>1</sup> D <sub>2</sub> )6p[3] <sub>7/2</sub>	12(9)	13(10)	75(10)		
(42)	( <sup>1</sup> D)6p <sup>2</sup> F <sub>7/2</sub>	2.3	1.7	96.0	-0.492	3.101
		1.7	2.0	96.3		

$$^a\delta_1 = \delta_{d_{5/2}} - \delta_{g_{9/2}}.$$

$$^b\delta_2 = \delta_{g_{7/2}} - \delta_{g_{9/2}}.$$

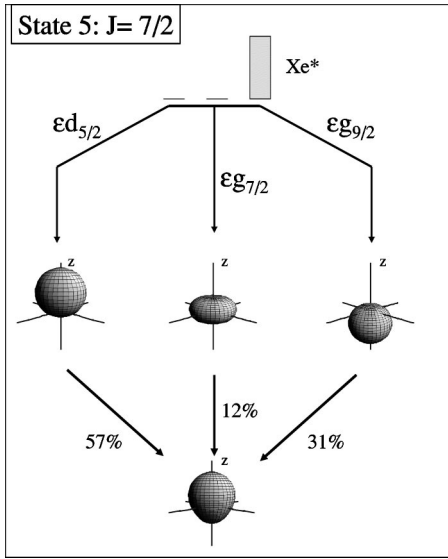


FIG. 3. An illustration of orientation transfer in the case of Auger decay to state 5 [ $\text{Xe}^{+*} ({}^3P_2)6p[3]_{7/2}$ ] using a semiclassical approximation [see Eq. (11)] to render a three-dimensional distribution of the magnetic sublevels for the residual ion.

case of Auger decay of the  $\text{Xe}^* 4d_{5/2}^{-1}6p(J^*=1)$  state into the ionic  $\text{Xe} \Pi 5p^4 6p$  states with total angular momentum  $J = \frac{1}{2}, \frac{3}{2}, \frac{5}{2}$ , and  $\frac{7}{2}$  are presented in the Appendix.

The anisotropy parameter  $\alpha_2$  has been measured in a few papers [14,27–31]. Higher energy resolution than in other experiments allowed Aksela *et al.* [31] and Langer *et al.* [14] to determine the anisotropy parameter for the individual

Auger transitions investigated in this paper. The spin-polarization parameter  $\xi_2$  has been measured for some of the resonant Auger lines of our interest by Hergenbahn *et al.* [22]. The difficulty of spin-polarization measurements, however, is the low collection efficiency and the resulting low resolution. Therefore completely resolved experimental data for all transitions are presently not available.

Figure 4 presents, in the complex plane, the relative Auger decay amplitudes for transition into the final ionic  $\text{Xe} \Pi 5p^4 6p$  states with  $J = \frac{1}{2}$ . The amplitudes, given by Eq. (2), are normalized by the condition  $|V_{s_{1/2}}|^2 + |V_{d_{3/2}}|^2 = 1$  and the phase  $\delta_{s_{1/2}}$  is chosen to be zero. The choice of  $\delta_{s_{1/2}}$  constricts  $V_{s_{1/2}}$  to be real and therefore the data for  $\Gamma_{s_{1/2}}$  in Table II (related to  $|V_{s_{1/2}}|$  by the expression  $\Gamma_{\ell j} = 2\pi |V_{\ell j}|^2$ ) are represented by a point with an error bar on the real axis. Since the fluorescence data give no information on the phase  $\delta_{d_{3/2}}$ , the data in Table II for  $\Gamma_{d_{3/2}}$  are represented by the two circles in the complex plane depicted in each plot. The error bars on this data are then given by the space between these two circles. In order to include the phase differences  $\delta_1$  in this presentation, the values of  $\cos(\delta_{s_{1/2}} - \delta_{d_{3/2}})$  were extracted using Eq. (A3) by substitution of the angular anisotropy parameters  $\alpha_2$  measured in Refs. [14,31] and our data on  $|V_{s_{1/2}}|/|V_{d_{3/2}}|$ . This gives the phase difference up to the sign. The error bars on the phase difference,  $\delta_{s_{1/2}} - \delta_{d_{3/2}}$ , were obtained by propagating the errors in the determination of the relative partial widths (Table II) as well as those in the measurement of  $\alpha_2$  [14,31].

Therefore the experimental data on the amplitudes for a final  $\text{Xe} \Pi$  state with  $J = \frac{1}{2}$  are displayed as a combination of

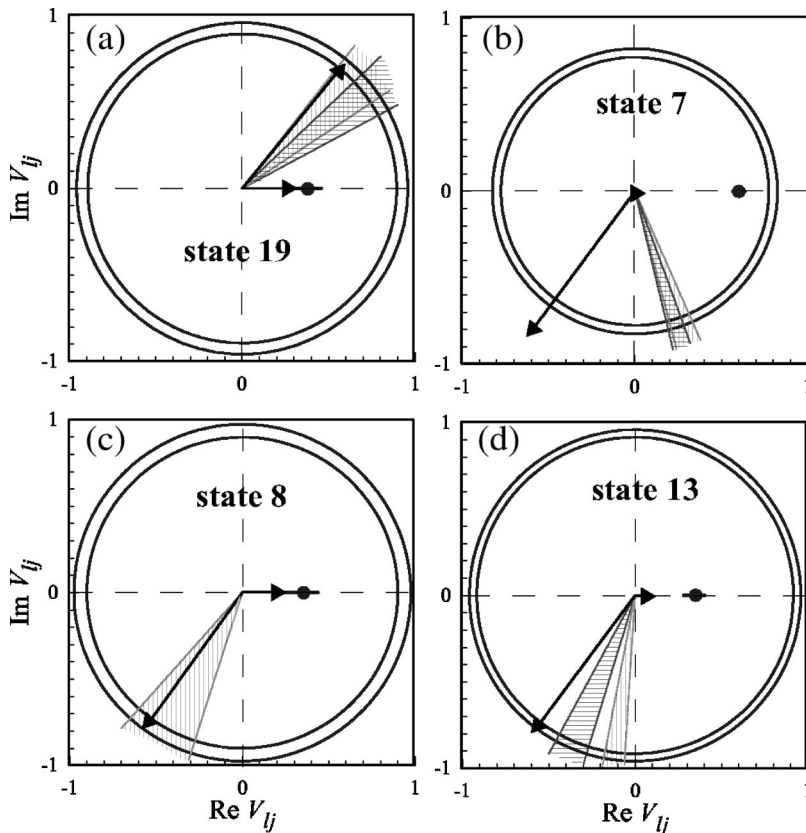


FIG. 4. Complex plane of the Auger decay amplitudes (2) for transitions to the ionic  $\text{Xe} \Pi 5p^4 6p$  states with  $J = \frac{1}{2}$ . The present data on the relative partial widths (point with error bars and circles) are complemented by the phase difference data extracted from the values of  $\alpha_2$  taken from Ref. [31] (area shaded by vertical stripes) and [14] (horizontal stripes) (see text). Vectors present theoretical results of model (e) for the  $V_{s_{1/2}}$  and  $V_{d_{3/2}}$  amplitudes. The  $V_{s_{1/2}}$  amplitude is chosen to be real.



the experimental point (with error bar) on the  $\text{Re } V_{\ell j}$  axis for the  $V_{s1/2}$  amplitude and the intersection of the rings with striped sectors for the  $V_{d3/2}$  amplitude. The angle between the real axis and the vector from the origin to the above intersection gives the complex phase. For the particular case of state no. 19, the positive sign of the relative phase follows experimentally from the spin polarization data [22,32], as shown in Fig. 4(a). For the other three states only the solutions with  $\text{Im } V_{d3/2} < 0$  are left on the plots in accordance with the theoretical calculations. Together with the results from Auger electron data, the present fluorescence data for the decay into the  $J=\frac{1}{2}$  states presented in Fig. 4 constitute the complete experiment: the relative complex Auger decay amplitudes are fully determined. The complex Auger decay amplitudes calculated using the theoretical model outlined in Sec. VI are represented by the bold vectors and will be discussed in that section. It should be noted that in these plots we do not present the Auger line no. 4, unresolved in Refs. [14,31], or the very weak line no. 20 because of large error bars (see Table II).

For the  $\text{Xe } \Pi 5p^46p$  states with  $J>\frac{1}{2}$ , when three decay amplitudes are involved, there are not enough data available in order to display the amplitudes in a transparent form within the complex plane. Therefore we use the following strategy: having determined the absolute relative amplitudes,  $|V_{\ell j}|/|V_{\ell' j'}|$ , in Sec. IV we introduce them into Eqs. (A6), (A7), (A10), (A11), (A14), and (A15) from the Appendix. This procedure yields equations with only three variables: either  $\alpha_2$  or  $\xi_2$  and the two phase differences  $\delta_1$  and  $\delta_2$  (see the Appendix for the notation of  $\delta_1$  and  $\delta_2$  specific for states with different  $J$ 's). In our case, however, only the  $\alpha_2$  parameters are available from the literature [14,31]. Introduction of these  $\alpha_2$  parameters into Eqs. (A6), (A10), and (A14) yields parametric relations between  $\delta_1$  and  $\delta_2$ . The black bold lines in the plots of  $\delta_1$  vs  $\delta_2$  in Figs. 5 and 6 are the graphical illustration of these parametric relations using the  $\alpha_2$  parameters from Ref. [31] [except for the plots Fig. 6(b) where the data of Ref. [14] are used due to their smaller error bars for this state]. The shaded area on these plots is the parameter space filled due to propagation of the error bars of the experimental determination of partial widths (see Tables III–V) and those of the Auger electron parameter  $\alpha_2$  from Refs. [14,31] together with the condition that  $\sum_{\ell j} \Gamma_{\ell j} / \Gamma = 1$ . If the value of at least one of the amplitudes is much smaller than the others, the relative phase of the small amplitude is not essential and actually cannot be extracted with high enough accuracy to be compared with theory. This situation is quite frequent, as is seen from Tables II–V. It is for this reason that Figs. 5 and 6 show only the selected examples, where the error bars in the reduced parameter space allow a meaningful comparison of experiment and theory.

Furthermore, one can show by calculating the Jacobians for sets of equations for  $\alpha_2$  and  $\xi_2$  with respect to  $\delta_1$  and  $\delta_2$ , that at each  $J$  the parameters  $\alpha_2$  and  $\xi_2$  are independent provided the absolute values of the amplitudes are nonvanishing. Therefore if the parameters  $\xi_2$  are available then Eqs. (A7), (A11), and (A15) can be reduced using the above procedure; a nontrivial solution occurs for  $\delta_1$  and  $\delta_2$  and the complete experiment can be, in principle, performed. Before

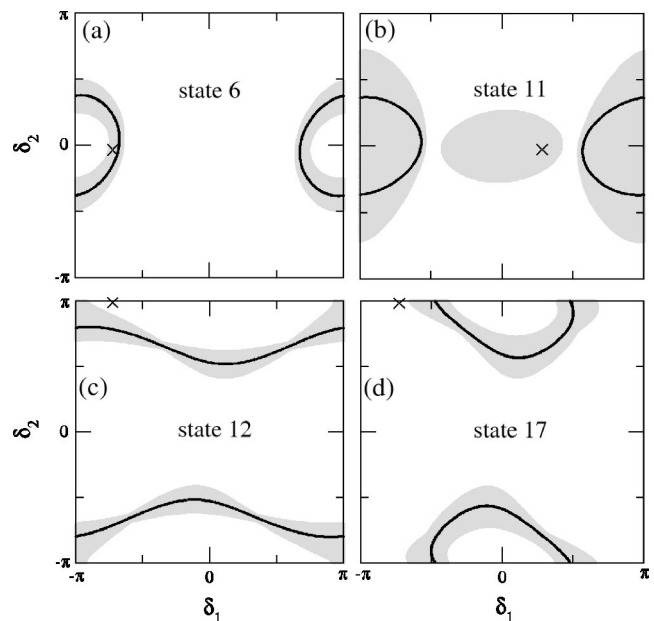


FIG. 5. The reduced parameter space  $\delta_2$  vs  $\delta_1$  found from a combination of the fluorescence polarization data and the Auger electron angular distribution parameter  $\alpha_2$  [14,31] for the final ionic  $\text{Xe } \Pi 5p^46p$  states with  $J=\frac{3}{2}$ . Results of model (e) are indicated by crosses (see text). The plots shown describe the phase differences in the Auger decay to the  $J=3/2$  states: (a) no. 6, (b) no. 11, (c) no. 12, and (d) no. 17.

analyzing the obtained results we turn to the theoretical description of the Auger decay amplitudes.

## VI. CALCULATION OF AUGER DECAY AMPLITUDES

Detailed information about the calculational procedure may be found, e.g., in Refs. [60,61]. In particular, the bound state wave functions of the Auger state  $\text{Xe}^* 4d_{5/2}^{-1}6p(J^*=1)$  and of the ionic final states  $\text{Xe } \Pi 5p^46p$  are constructed using the multiconfigurational Dirac-Fock (MCDHF) computer code GRASP92 [62]. Intermediate coupling and configuration mixing were taken into account for the ionic states, while the Auger state  $4d_{5/2}^{-1}6p(J^*=1)$  is very well described in a pure coupling single-configuration approximation [45]. To follow the evolution of the results, when new ionic configurations are included, we have performed a series of computations by increasing stepwise the number of ionic configurations in the wave-function expansions: (a)  $5p^46p$  (single-configuration model), (b)  $5p^46p+5p^47p$ , (c)  $5p^46p+5p^47p+5p^5$ , (d)  $5p^46p+5p^47p+5p^5+5p^36p^2+5s^{-2}5p^66p$ , and (e)  $5p^46p+5p^47p+5p^5+5p^36p^2+5s^{-2}5p^66p+5p^44f$ . In order to calculate the Auger amplitudes, separately optimized orbital functions from the initial and final ionic states were used and hence include some of the relaxation effects. However, no attempts have been made to incorporate completely the non-orthogonality effects into the computations. Model (e), which we use as the final model in our calculations, is close to those of Tulkki *et al.* [45] and Aksela *et al.* [15] (FE model), except that a larger set of configuration state functions is used in the representation of the ionic states. The

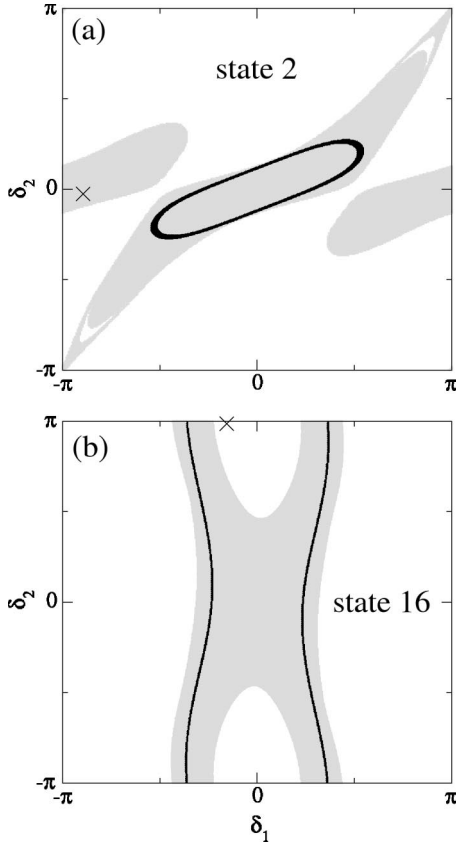


FIG. 6. Same as Fig. 5 but for (a) the final state no. 2 with  $J = \frac{5}{2}$  and (b) that with  $J = \frac{7}{2}$  (state no. 16).

computations differ also slightly in the generation of the bound and continuum orbitals.

For the calculation of the continuum wave functions we solved the one-electron MCDHF equations for each final scattering state with angular momentum  $\vec{J}_{tot} = \vec{J} + \vec{j}$  separately taking into account the proper direct and exchange potentials [63]. For these continuum functions orthogonality is enforced with respect to the bound state orbitals of the same symmetry but is obtained automatically for different symmetries of the continuum orbitals as well as for different  $J_{tot}$  owing to the angular momentum selection rules. Each continuum orbital is therefore used for exactly one many-electron Auger decay amplitude (2). The normalization and the phase shifts (scattering phases) of the continuum orbitals are deduced using the WKB method [64].

The phase shifts  $\varphi_{\ell j}$  are determined by the (energy-normalized) asymptotic behavior of the continuum wave functions,  $p^{-1/2} \sin(pr - \pi\ell/2 - p \ln 2pr + \varphi_{\ell j})$ , where  $p = \sqrt{\varepsilon(\text{Ry})}$ . These shifts are important for the description of the Auger electron parameters. In the Condon-Shortley phase convention used here the Auger decay amplitudes (2) can be written in the form  $V_{\ell j} = i^\ell \exp(-i\varphi_{\ell j}) u_{\ell j}$ , where  $u_{\ell j}$  refers to the real reduced matrix element of the electron-electron interaction between the initial bound and the final scattering state, and is built up from Slater integrals and angular coupling coefficients. The scattering phases  $\varphi_{\ell j}$  are related to the phases of the decay amplitudes  $\delta_{\ell j}$  in Eq. (2) by

$$\delta_{\ell j} = -\varphi_{\ell j} + \frac{\pi\ell}{2} + (1 - \text{sgn } u_{\ell j}) \frac{\pi}{2}, \quad (16)$$

where  $\text{sgn } x = 1$  if  $x \geq 0$  and  $\text{sgn } x = -1$  if  $x < 0$ . Tables II–V contain the relative partial decay widths  $\Gamma_{\ell j}/\Gamma$  and the phase differences  $\delta_{\ell j} - \delta_{\ell' j'}$  [defined in the interval  $(-\pi, \pi)$ ] in model (e), allowing calculation of any relative observable quantity for the resonance Auger decay (1a)–(1b). Note that the variation of the relative phases  $\delta_1$  and  $\delta_2$  by  $\pi$  from state to state (see Tables II–V) are caused by the last term in Eq. (16). The relative phase  $\delta_2$  is due to the relativistic effects, which cause differences between the electron continuum wave functions with the same  $\ell$  and different  $j$ :  $\delta_2$  reduces to 0 or  $\pm\pi$  provided the relativistic effects are negligible. In our calculations  $\delta_2$  deviates from these values only within  $5^\circ$ , pointing to a small influence of relativistic effects on the outgoing electron waves.

Table VI presents the branching ratios of the Xe II  $5p^4 6p$  Auger lines. The corresponding high-resolution data were obtained in Refs. [14,15]. Our calculations are in good agreement with other theoretical MCDHF-based calculations [15,43–45], but deviate substantially for some lines from Refs. [47,48]. These deviations can be attributed to a less sophisticated treatment of the Auger electron-residual ion interaction in Refs. [47,48]: neglecting the small components and using a semiempirical form of the scattering potential. Although already the single-configuration model (a) reproduces the experimental relative Auger line strength quite satisfactorily, including new ionic configurations generally improves the agreement with experimental data (states 3, 7, 8, 9, 17, 18). Despite the overall good agreement between theory and experiment, there is one striking discrepancy for the  $5p^4(^1D_2)6p[3]_{7/2}$  state (no. 16). None of the calculations can reproduce the small decay rate into this state as derived from experimental data. Therefore it is hard to expect reliable results for other Auger decay parameters for this final ionic state. Accounting for the final ion configuration mixing reduces the total Auger decay width of the  $4d_{5/2}^{-1} 6p(J^* = 1)$  state to the Xe II  $5p^6 6p$  manifold by about 15%: from  $9.75 \times 10^{13} \text{ sec}^{-1}$  in model (a) to  $8.43 \times 10^{13} \text{ sec}^{-1}$  in model (e).

## VII. DISCUSSION

Our theoretical and experimental results for the relative partial widths (Tables II–V) are in a good qualitative and often quantitative agreement, except for a few cases. The theoretical results are also in accord with the calculations of Lagutin *et al.* [16]: the only exception is the extremely weak line no. 20 (Table II), which is strictly forbidden in the pure coupling single configuration approximation and is very sensitive to small details of the theoretical models. Experimental data for this state were obtained with large error bars and we omit state no. 20 from the following discussion. The configuration mixing only weakly influences the branching ratios between the different partial widths, therefore it is not illustrated here. Especially stable are the results for the states with  $J = \frac{5}{2}$  and  $\frac{7}{2}$ , when the  $s$  wave does not contribute to the decay. Although some states (nos. 4, 8, 11, 12) with  $J = \frac{1}{2}$  and  $\frac{3}{2}$  show variations of the branching ratios when introducing

TABLE VI. Branching ratios of the Auger lines in the resonant decay  $\text{Xe}^* 4d_{5/2}^{-1}6p(J^*=1) \rightarrow \text{Xe II } 5p^4 6p + e_A^-$ .

No.	Final state	This work					Experiment		Theory			
		(a)	(b)	(c)	(d)	(e)	[15]	[14]	[15,45]	[44]	[43]	[47,48]
1	$(^3P_2)6p[2]_{3/2}$	0.41	0.39	0.56	0.62	0.62	1.03	0.30	0.69	0.55	0.51	9.22
2	$(^3P_2)6p[2]_{5/2}$	3.28	3.65	3.65	3.88	3.88	2.66	3.49	3.24	4.17	3.96	0.08
3	$(^3P_2)6p[3]_{5/2}$	4.67	4.98	4.98	5.20	5.29	6.09	5.65	4.62	5.82	6.17	10.89
4	$(^3P_2)6p[1]_{1/2}$	0.72	0.82	0.70	0.73	0.74	0.65	} 2.57 <sup>a</sup>	0.87	0.86	0.87	0.66
5	$(^3P_2)6p[3]_{7/2}$	1.89	2.05	2.05	2.16	2.18	1.36		2.48	1.62	1.63	1.17
6	$(^3P_2)6p[1]_{3/2}$	12.51	13.95	11.83	12.33	12.45	15.20	15.05	9.13	15.56	15.55	7.93
7	$(^3P_0)6p[1]_{1/2}$	1.28	1.39	1.25	0.70	0.63	0.62	0.73	0.69	0.86	0.81	0.39
8	$(^3P_1)6p[0]_{1/2}$	0.32	0.35	0.31	0.82	0.90	0.90	1.07	0.75	1.27	1.21	0.57
9	$(^3P_0)6p[1]_{3/2}$	3.22	3.43	3.75	5.76	5.84	6.57	6.44	5.60	6.27	6.62	3.35
10	$(^3P_1)6p[2]_{5/2}$	0.17	0.20	0.20	0.21	0.21	0.13	0.20	0.17	0.24	0.22	0.12
11	$(^3P_1)6p[2]_{3/2}$	3.58	3.96	2.98	2.61	2.79	3.70	3.61	2.43	3.00	3.31	2.16
12	$(^3P_1)6p[1]_{3/2}$	2.57	2.93	3.35	2.67	2.58	2.84	3.33 <sup>a</sup>	2.14	3.37	2.94	1.36
13	$(^3P_1)6p[1]_{1/2}$	1.97	2.26	1.93	2.19	2.19	2.54	2.94	1.91	3.03	3.09	8.04
14	$(^1D_2)6p[3]_{5/2}$	0.56	0.60	0.60	0.63	0.65	0.25	0.32	0.58	0.55	0.54	6.01
15	$(^1D_2)6p[1]_{3/2}$	10.20	9.60	10.61	10.77	10.91	13.60	12.45	13.11	10.67	10.35	0.07
16	$(^1D_2)6p[3]_{7/2}$	14.97	16.29	16.29	17.15	17.07	2.44	3.66	21.09	10.33	10.09	9.18
17	$(^1D_2)6p[2]_{3/2}$	5.36	6.45	5.71	6.12	6.07	6.79	5.87	3.76	5.89	6.06	18.33
18	$(^1D_2)6p[2]_{5/2}$	6.31	6.76	6.76	7.12	7.11	7.48	7.68	6.99	6.68	6.72	1.65
19	$(^1D_2)6p[1]_{1/2}$	6.25	6.30	6.20	6.57	6.63	9.88	9.50	6.76	6.78	6.72	5.58
20	$(^1S_0)6p[1]_{1/2}$	0.00	0.00	0.00	0.01	0.01	0.24	0.24	0.00	0.00	0.00	0.04
21	$(^1S_0)6p[1]_{3/2}$	19.69	13.61	15.40	11.74	11.24	15.04	14.89	13.00	12.57	12.61	13.22

<sup>a</sup>Not resolved.

new configurations, most of the changes remain moderate. As an example where strong variation occurs: adding the  $5p^5$  configuration [model (c)] changes the branching ratio,  $\Gamma_{s_{1/2}}:\Gamma_{d_{3/2}}:\Gamma_{d_{5/2}}$ , for state no. 12 (see Table III) from 0.1:56.7:43.2 [model (b)] to 0.0:36.4:63.5, while adding the configurations  $5p^3 6p^2$  and  $5s^{-2} 5p^6 6p$  in model (d) brings this branching ratio (0.1:61.1:38.9) almost back to the final one [model (e)]. Theoretical branching ratios for the majority of states can be qualitatively understood on the basis of the nonrelativistic strict spectator model, when the Auger transition effectively proceeds within the ionic core:  $4d_{5/2}^{-1} 5p^6 \rightarrow 5p^4 + \varepsilon \ell j$ , i.e., without any interaction with the  $6p$  electron. The dominance of the  $\varepsilon d$  channels for the vast majority of states in Tables II–V is then partly explained by the fact that the Auger decay into the  $\varepsilon s$  and  $\varepsilon g$  channels is forbidden for the  $5p^4 \ ^3P$  and  $5p^4 \ ^1S$  core states of the residual ion. Examples of the analysis for the partial Auger widths were given in Ref. [32].

Despite the general agreement of experiment and theory, there are a few deviations showing that there is room for more sophisticated models of the resonant Auger process considered. For example, for the state  $5p^4(^1D_2)6p[3]_{7/2}$  (no. 16), the main reason of the above-mentioned large disagreement between theory and experiment for the decay rate (see Table VI) is an overestimation of the contribution from the  $\varepsilon g_{9/2}$  channel (see Table V). The overestimate of the  $g$  channel appears to be a regularity (see states 5, 18), which points

to an effect not included in the theoretical calculations.

More information can be gained from the complex Auger decay amplitudes. Figure 4 visualizes the relation between theory and experiment on the level of the decay amplitudes for the ionic states with  $J=\frac{1}{2}$ . Experiment and theory are in a good agreement for the states  $(^1D_2)6p[1]_{1/2}$  (no. 19) and  $(^3P_1)6p[0]_{1/2}$  (no. 8), while there are disagreements in both the relative phase and the absolute amplitudes' ratio for the states 7 and 13. Note that for state 8 no part of the amplitude complex plane satisfies simultaneously the anisotropy parameter  $\alpha_2$  determined in Ref. [14] and our measurements (the corresponding  $\alpha_2$  parameters in Refs. [14,31] are also in contradiction) and that only data from Ref. [31] are used in Fig. 4(c). The calculated relative phases (not the phases themselves) are only slightly dependent on the number of accounted final ionic configurations: models (a) and (e) exhibit not more than a  $2^\circ$  difference in  $\varphi_{s_{1/2}} - \varphi_{d_{3/2}}$ . Disagreement in the relative phases are likely related to the simple one-electron model for the continuum Auger electron. An additional argument for the latter statement follows from results of the complete experiment for the normal Auger decay in sodium,  $\text{Na}^+(2s2p^6 4p^3 P) \rightarrow \text{Na}^{++}(2s^2 2p^5 P) + e_A^-(s, d)$  [40]. In this example the improvement of the description of the ionic core crucially changed the branching ratio, but did not influence the phase difference,  $\varphi_s - \varphi_d$ . Note that the values of  $\delta_{s_{1/2}} - \delta_{d_{3/2}}$  are not far from  $\pm\pi/2$ , which can result in a large dynamic spin polarization of the Auger electrons in



accordance with the propensity rules discussed in Refs. [47,65].

Experimental and theoretical data, shown as crosses, on the final states Xe II  $5p^46p$  with  $J > \frac{1}{2}$  are compared in Fig. 5 ( $J = \frac{3}{2}$ ) and Fig. 6 ( $J = \frac{5}{2}, \frac{7}{2}$ ). When discussing the shape of these plots it should be considered that they are the result of the combination of the parameters  $\eta_1$ ,  $\eta_2$ , and  $\alpha_2$  with Eqs. (A6), (A10), and (A14). Taking, for example, Fig. 5, it can be seen that the reduced parameter space for states 6 and 11 is centered around  $\delta_2 = 0$  (in agreement with the theoretical predictions). These plots correspond to a negative  $\alpha_2$  and  $\eta_2 \ll 1$  ( $\eta_1$  is always small for decay to states with  $J = \frac{3}{2}$  due to the small relative amplitude of the  $\epsilon s_{1/2}$  wave for all states, see Table III). On the other hand, for states 12 and 17 the reduced parameter space is centered around  $\delta_2 = \pm \pi$  (again in agreement with theory) and corresponds to a positive  $\alpha_2$  and  $\eta_2 \approx 1$ . Furthermore, there is some correlation between the values of  $\alpha_2$  and  $\eta_2$ . For example, if  $\alpha_2$  is strongly negative and  $\eta_2 \approx 1$ , no values of  $\delta_1$  and  $\delta_2$  can be found to satisfy Eq. (A6) (likewise for strongly positive values of  $\alpha_2$  and  $\eta_2 \ll 1$ ). The fact that the combination of experimental values gives a reduced parameter space in these plots is a demonstration of their consistency. Similar discussions can be made for the plots involving decay to states with  $J = \frac{5}{2}, \frac{7}{2}$  although  $\alpha_2$  is expressed in a less simple way. The complete set of data can be deduced provided the present data can be combined with similar plots based on the relation between  $\xi_2$ ,  $\eta_1$ , and  $\eta_2$  [using Eqs. (A7), (A11), and (A15) in the Appendix].

The error bars for  $\delta_1$  and  $\delta_2$  can be read from Fig. 5. Taking, for example, state 6 shown in Fig. 5(a),  $\delta_1$  is constrained to the intervals  $(-\pi, -\pi + 1.1)$  and  $(\pi, \pi - 1.1)$  while  $\delta_2 = 0.0 \pm 1.5$ . These error bars are still rather large in spite of the reduced parameter space shown in the figure. However, by assuming vanishing relativistic effects (i.e.,  $\delta_2 = 0$  for this state), it is even possible to obtain a rather accurate phase difference (except the sign):  $\delta_1 = \pm(2.1^{+0.2}_{-0.1})$ .

Generally, there is a good correlation between the calculations and the phase parameter plots: the theoretical results fit or almost fit into the reduced parameter space. Similar to the case of  $J = \frac{1}{2}$ , the sensitivity of the calculations to inclusion of more ionic configurations is small (not shown): the relativistic splitting, the  $\delta_2$  parameter, remains always small or close to  $\pm \pi$ , while the phase difference between the continuum electron waves with different  $\ell$ , the  $\delta_1$  parameter, changes only slightly, especially for the states with  $J = \frac{5}{2}$  and  $\frac{7}{2}$ . The latter is in accordance with the discussion of the branching ratios and can be attributed to the fact that correlations within the ionic core have a stronger effect on the  $s$  wave, which is more localized near the nucleus than the  $d$  and  $g$  waves subjected to the repulsive centrifugal force. Note that despite some qualitative disagreements in the relative partial widths between theory and experiment (states 11, 2, and 16 in Tables III–V) and especially the crucial disagreement in the relative intensity of the Auger line no. 16 (Table VI), the relative phases of the decay amplitudes for these states are still within the error bars. This explicitly demonstrates that only use of the complete set of data can evaluate the validity of a theoretical model.

In Refs. [47,65] the destructive interference between the three emitted partial waves has been suggested as a mecha-

nism of decreasing the dynamic spin polarization of the Auger electrons in the resonant Auger decay process (1a)–(1b) for the final ionic states with  $J > \frac{1}{2}$ . Close inspection of the present results leads to a more accurate conclusion. For states with  $J = \frac{3}{2}$  and  $J = \frac{5}{2}$  only two decay channels dominate,  $\epsilon d_{3/2}$  and  $\epsilon d_{5/2}$  ( $\eta_1 \ll 1$ ), with a small relativistic splitting between the phases of the corresponding amplitudes ( $\delta_2 \ll 1$ ). Then it follows from Eqs. (A7) and (A11) that  $\xi_2 \ll 1$ . This situation corresponds to two decay channels with a small phase difference between the two amplitudes and has been analyzed a long time ago [66].

## VIII. CONCLUSION

The relative partial widths of the resonant Auger decay to almost all final Xe II states of the  $5p^46p$  configuration have been measured by means of fluorescence polarimetry in combination with resonance photoionization by both linearly and circularly polarized synchrotron radiation. Combination of these data with the data from the angular resolved Auger electron spectroscopy allowed the determination of the complex relative partial decay amplitudes for the states with  $J = \frac{1}{2}$  and therefore the complete experiment to be performed. We proved that with our measurements and analysis of the fluorescence polarization after the Auger decay the complete experiment is possible for the final ionic states with  $J > \frac{1}{2}$ , when three decay channels contribute. The present analysis results in a significant reduction of the amplitudes' parameter space and in a substantial contribution to the complete experiment for the states with  $J > \frac{1}{2}$ . Our theoretical calculations based on the relativistic multiconfigurational Dirac-Fock model are generally in a good agreement with the experimental data, although further improvements of the model are needed to achieve better agreement. We found that the theoretical results are rather stable with respect to mixing of configurations in the final ionic states and the most important improvement is expected to arise from a more precise description of the Auger electron continuum wave functions. The developed method can be used for performing complete experiments in photoionization when the photoion remains in an excited state decaying by radiation emission.

## ACKNOWLEDGMENTS

We wish to thank S. Turchini for advice and help in beam-line operation at ELETTRA as well as T. Marin for help in setting up the experiment. The experimental work was supported by the European Community under Contract No. HPRI-CT-1999-00033. A.N.G. gratefully acknowledges the hospitality of LURE, the financial support of the CNRS and the University of Paris—Sud, and the support provided by the Russian Foundation for Basic Research under Grant No. 04-02-17236. S.F. would like to acknowledge support from the Deutsche Forschungsgemeinschaft (DFG) under Contract No. FR 1251 8-1.

## APPENDIX

Below are presented explicit expressions for the parameters (10), (13), and (15) in terms of the partial amplitudes of



the Auger decay  $4d_{5/2}^{-1}6p(J^*=1) \rightarrow 5p^46p(J) + \varepsilon \ell j$ . Notations for  $\delta_1$  and  $\delta_2$  coincide with the notations in Tables II–V. We use the notations  $N=1+\eta_1^2$  for  $J=\frac{1}{2}$  and  $N=1+\eta_1^2+\eta_2^2$  for  $J=\frac{3}{2}, \frac{5}{2}, \frac{7}{2}$ .

$J=1/2$ . Decay channels:  $\varepsilon s_{1/2}, \varepsilon d_{3/2}$ ,

$$\delta_1 = \delta_{s_{1/2}} - \delta_{d_{3/2}}, \quad \eta_1 = |V_{s_{1/2}}|/|V_{d_{3/2}}|, \quad (\text{A1})$$

$$\mathcal{A}_{10} = \frac{1}{2N}(2\eta_1^2 - 1), \quad (\text{A2})$$

$$\alpha_2 = -\frac{1}{\sqrt{2}N}(1 + 2\sqrt{2}\eta_1 \cos \delta_1), \quad \xi_2 = \frac{3}{N}\eta_1 \sin \delta_1. \quad (\text{A3})$$

$J=3/2$ . Decay channels:  $\varepsilon s_{1/2}, \varepsilon d_{3/2}, \varepsilon d_{5/2}$ ,

$$\delta_1 = \delta_{s_{1/2}} - \delta_{d_{5/2}}, \quad \eta_1 = |V_{s_{1/2}}|/|V_{d_{5/2}}|, \quad \delta_2 = \delta_{d_{3/2}} - \delta_{d_{5/2}},$$

$$\eta_2 = |V_{d_{3/2}}|/|V_{d_{5/2}}|, \quad (\text{A4})$$

$$\mathcal{A}_{10} = \frac{\sqrt{5}}{10N}(5\eta_1^2 + 2\eta_2^2 - 3), \quad \mathcal{A}_{20} = \frac{1}{10N}(5\eta_1^2 - 4\eta_2^2 + 1), \quad (\text{A5})$$

$$\alpha_2 = \frac{\sqrt{2}}{5N}[2\eta_2^2 - 2 + 3\sqrt{5}\eta_1 \cos \delta_1 - 3\eta_2 \cos \delta_2$$

$$+ \sqrt{5}\eta_1 \eta_2 \cos(\delta_1 - \delta_2)], \quad (\text{A6})$$

$$\xi_2 = -\frac{3}{2\sqrt{10}N}[-2\eta_1 \sin \delta_1 + \sqrt{5}\eta_2 \sin \delta_2 + \eta_1 \eta_2 \sin(\delta_1 - \delta_2)]. \quad (\text{A7})$$

$J=5/2$ . Decay channels:  $\varepsilon d_{3/2}, \varepsilon d_{5/2}, \varepsilon g_{7/2}$ ,

$$\delta_1 = \delta_{g_{7/2}} - \delta_{d_{5/2}}, \quad \eta_1 = |V_{g_{7/2}}|/|V_{d_{5/2}}|, \quad \delta_2 = \delta_{d_{3/2}} - \delta_{d_{5/2}},$$

$$\eta_2 = |V_{d_{3/2}}|/|V_{d_{5/2}}|, \quad (\text{A8})$$

$$\mathcal{A}_{10} = \frac{\sqrt{3}}{2\sqrt{35}N}(-5\eta_1^2 + 7\eta_2^2 + 2),$$

$$\mathcal{A}_{20} = \frac{1}{10\sqrt{14}N}(5\eta_1^2 + 14\eta_2^2 - 16), \quad (\text{A9})$$

$$\alpha_2 = \frac{1}{35\sqrt{2}N}[-25\eta_1^2 - 7\eta_2^2 + 32 - 12\sqrt{5}\eta_1 \cos \delta_1$$

$$+ 6\sqrt{14}\eta_2 \cos \delta_2 + 12\sqrt{70}\eta_1 \eta_2 \cos(\delta_1 - \delta_2)], \quad (\text{A10})$$

$$\xi_2 = \frac{3}{2\sqrt{35}N}[-\sqrt{14}\eta_1 \sin \delta_1 + \sqrt{5}\eta_2 \sin \delta_2$$

$$+ 4\eta_1 \eta_2 \sin(\delta_1 - \delta_2)]. \quad (\text{A11})$$

$J=7/2$ . Decay channels:  $\varepsilon d_{5/2}, \varepsilon g_{7/2}, \varepsilon g_{9/2}$ ,

$$\delta_1 = \delta_{d_{5/2}} - \delta_{g_{9/2}}, \quad \eta_1 = |V_{d_{5/2}}|/|V_{g_{9/2}}|, \quad \delta_2 = \delta_{g_{7/2}} - \delta_{g_{9/2}},$$

$$\eta_2 = |V_{g_{7/2}}|/|V_{g_{9/2}}|, \quad (\text{A12})$$

$$\mathcal{A}_{10} = \frac{1}{2\sqrt{21}N}(9\eta_1^2 + 2\eta_2^2 - 7),$$

$$\mathcal{A}_{20} = \frac{1}{10\sqrt{21}N}(15\eta_1^2 - 20\eta_2^2 + 7), \quad (\text{A13})$$

$$\alpha_2 = \frac{\sqrt{2}}{21N}[-3\eta_1^2 + 10\eta_2^2 - 7 + 3\sqrt{105}\eta_1 \cos \delta_1 - \sqrt{35}\eta_2 \cos \delta_2$$

$$+ 3\sqrt{3}\eta_1 \eta_2 \cos(\delta_1 - \delta_2)], \quad (\text{A14})$$

$$\xi_2 = \frac{\sqrt{3}}{2\sqrt{14}N}[+2\sqrt{5}\eta_1 \sin \delta_1 - \sqrt{15}\eta_2 \sin \delta_2$$

$$- \sqrt{7}\eta_1 \eta_2 \sin(\delta_1 - \delta_2)]. \quad (\text{A15})$$

- 
- [1] *Complete Scattering Experiments*, edited by U. Becker and A. Crowe (Kluwer Academic/Plenum Publishers, New York, 2001).
- [2] G. B. Armen, H. Aksela, T. Åberg, and S. Aksela, J. Phys. B **33**, R49 (2000), and references therein.
- [3] W. Mehlhorn, in *X-ray and Inner-Shell Processes*, edited by T. A. Carlson, M. O. Krause, and S. T. Manson, AIP Conf. Proc. No. 215 (AIP, New York, 1990), p. 465.
- [4] N. M. Kabachnik and I. P. Sazhina, J. Phys. B **23**, L353 (1990).
- [5] W. Eberhardt, G. Kalkoffen, and C. Kunz, Phys. Rev. Lett. **41**, 156 (1978).
- [6] V. Schmidt, S. Krummacher, F. Wuilleumier, and P. Dhez, Phys. Rev. A **24**, 1803 (1981).
- [7] S. Southworth, U. Becker, C. M. Truesdale, P. H. Kobrin, D.

- W. Lindle, S. Owaki, and D. A. Shirley, Phys. Rev. A **28**, 261 (1983).
- [8] U. Becker, T. Prescher, E. Schmidt, B. Sonntag, and H.-E. Wetzel, Phys. Rev. A **33**, 3891 (1986).
- [9] U. Becker, D. Szostak, M. Kupsch, H. G. Kerkhoff, B. Langer, and R. Wehlitz, J. Phys. B **22**, 749 (1989).
- [10] A. Kivimäki, A. Naves de Brito, S. Aksela, H. Aksela, O.-P. Sairanen, A. Ausmees, S. J. Osborne, L. B. Dantas, and S. Svensson, Phys. Rev. Lett. **71**, 4307 (1993).
- [11] H. Aksela, S. Aksela, G. M. Bancroft, K. H. Tan, and H. Pulkkinen, Phys. Rev. A **33**, 3867 (1986).
- [12] H. Aksela, S. Aksela, O.-P. Sairanen, A. Kivimäki, A. Naves de Brito, E. Nömmiste, J. Tulkki, S. Svensson, A. Ausmees, and S. J. Osborne, Phys. Rev. A **49**, R4269 (1994).
- [13] G. Öhrwall, J. Bozek, and P. Baltzer, J. Electron Spectrosc.

- Relat. Phenom. **104**, 209 (1999).
- [14] B. Langer, N. Berrah, A. Farhat, O. Hemmers, and J. D. Bozek, Phys. Rev. A **53**, R1946 (1996).
- [15] H. Aksela, O.-P. Sairanen, S. Aksela, A. Kivimäki, A. Naves de Brito, E. Nömmiste, J. Tulkki, A. Ausmees, S. J. Osborne, and S. Svensson, Phys. Rev. A **51**, 1291 (1995).
- [16] B. M. Lagutin, I. D. Petrov, Ph. V. Demekhin, V. L. Sukhorukov, F. Vollweiler, H. Liebel, A. Ehresmann, S. Lauer, H. Schmoranzner, O. Wilhelmi, B. Zimmermann, and K.-H. Schartner, J. Phys. B **33**, 1337 (2000).
- [17] M. Meyer, A. Marquette, A. N. Grum-Grzhimailo, U. Kleiman, and B. Lohmann, Phys. Rev. A **64**, 022703 (2001).
- [18] R. Kuntze, M. Salzmann, N. Böwering, and U. Heinzmann, Phys. Rev. Lett. **70**, 3716 (1993).
- [19] G. Snell, M. Drescher, N. Müller, U. Heinzmann, U. Hergenhahn, J. Viehhaus, F. Heiser, U. Becker, and N. B. Brookes, Phys. Rev. Lett. **76**, 3923 (1996).
- [20] G. Snell, B. Langer, M. Drescher, N. Müller, B. Zimmermann, U. Hergenhahn, J. Viehhaus, U. Heinzmann, and U. Becker, Phys. Rev. Lett. **82**, 2480 (1999).
- [21] B. Schmidtke, M. Drescher, N. A. Cherepkov, and U. Heinzmann, J. Phys. B **33**, 2451 (2000).
- [22] U. Hergenhahn, G. Snell, M. Drescher, B. Schmidtke, N. Müller, U. Heinzmann, M. Wiedenhöft, and U. Becker, Phys. Rev. Lett. **82**, 5020 (1999).
- [23] B. Schmidtke, T. Khalil, M. Drescher, N. Müller, N. M. Kabachnik, and U. Heinzmann, J. Phys. B **33**, 5225 (2000).
- [24] B. Schmidtke, T. Khalil, M. Drescher, N. Müller, N. M. Kabachnik, and U. Heinzmann, J. Phys. B **34**, 4293 (2001).
- [25] G. Snell, U. Hergenhahn, N. Müller, M. Drescher, J. Viehhaus, U. Becker, and U. Heinzmann, Phys. Rev. A **63**, 032712 (2001).
- [26] G. Snell, B. Langer, A. T. Young, and N. Berrah, Phys. Rev. A **66**, 022701 (2002).
- [27] T. A. Carlson, D. R. Mullins, C. E. Beall, B. W. Yates, J. W. Taylor, D. W. Lindle, and F. A. Grimm, Phys. Rev. A **39**, 1170 (1989).
- [28] B. Kämmerling, B. Krässig, and V. Schmidt, J. Phys. B **23**, 4487 (1990).
- [29] C. D. Caldwell and S. Hallman, Phys. Rev. A **53**, 3344 (1996).
- [30] N. Berrah and B. Langer, Comments At. Mol. Phys. **33**, 325 (1997).
- [31] H. Aksela, J. Jauhiainen, E. Nömmiste, O.-P. Sairanen, J. Karvonen, E. Kukk, and S. Aksela, Phys. Rev. A **54**, 2874 (1996).
- [32] P. O'Keeffe, S. Aloïse, M. Meyer, and A. N. Grum-Grzhimailo, Phys. Rev. Lett. **90**, 023002 (2003).
- [33] U. Becker, J. Electron Spectrosc. Relat. Phenom. **96**, 105 (1998).
- [34] N. A. Cherepkov and S. K. Semenov, J. Phys. B **37**, 1267 (2004).
- [35] B. M. Lagutin, I. D. Petrov, V. L. Sukhorukov, Ph. V. Demekhin, B. Zimmermann, S. Mickat, S. Kammer, K.-H. Schartner, A. Ehresmann, Yu. A. Shutov, and H. Schmoranzner, J. Phys. B **36**, 3251 (2003).
- [36] Obtaining only relative amplitudes instead of their absolute values may be referred to as "almost complete" experiment [40].
- [37] N. M. Kabachnik and A. N. Grum-Grzhimailo, J. Phys. B **34**, L63 (2001).
- [38] K. Ueda, Y. Shimizu, H. Chiba, Y. Sato, M. Kitajima, H. Tanaka, and N. M. Kabachnik, Phys. Rev. Lett. **83**, 5463 (1999).
- [39] A. N. Grum-Grzhimailo, A. Dorn, and W. Mehlhorn, Comments Mod. Phys. **1**, 29 (1999).
- [40] A. N. Grum-Grzhimailo, A. Dorn, and W. Mehlhorn, in *Complete Scattering Experiments*, edited by U. Becker and A. Crowe (Kluwer Academic/Plenum Publishers, New York, 2001), p. 111.
- [41] J. B. West, K. J. Ross, and H. J. Beyer, J. Phys. B **31**, L647 (1998).
- [42] K. Ueda, J. B. West, K. J. Ross, H.-J. Beyer, and N. M. Kabachnik, J. Phys. B **31**, 4801 (1998).
- [43] S. Fritzsche, Phys. Lett. A **180**, 262 (1993).
- [44] M. H. Chen, Phys. Rev. A **47**, 3733 (1993).
- [45] J. Tulkki, H. Aksela, and N. M. Kabachnik, Phys. Rev. A **50**, 2366 (1994).
- [46] U. Hergenhahn and U. Becker, J. Electron Spectrosc. Relat. Phenom. **76**, 225 (1995).
- [47] B. Lohmann, Aust. J. Phys. **52**, 397 (1999).
- [48] B. Lohmann and U. Kleiman, in *Many-Particle Spectroscopy of Atoms, Molecules, Clusters and Surfaces*, edited by J. Berakdar and J. Kirschner (Kluwer Academic/Plenum Publishers, New York, 2001), p. 173.
- [49] U. Hergenhahn, B. Lohmann, N. M. Kabachnik, and U. Becker, J. Phys. B **26**, L117 (1993).
- [50] J. E. Hansen and W. Persson, Phys. Scr. **36**, 602 (1987).
- [51] W. Persson, C.-G. Wahlström, G. Bertucci, H. O. Di Rocco, J. G. Reyna Almandos, and M. Gallardo, Phys. Scr. **38**, 347 (1988).
- [52] V. V. Balashov, A. N. Grum-Grzhimailo, and N. M. Kabachnik, *Polarization and Correlation Phenomena in Atomic Collisions: A Practical Theory Course* (Kluwer Academic/Plenum Publishers, New York, 2000).
- [53] N. M. Kabachnik, I. P. Sazhina, and K. Ueda, J. Phys. B **32**, 1769 (1999).
- [54] K. Blum, *Density Matrix Theory and Applications* (Plenum, New York, 1996).
- [55] N. M. Kabachnik and O. V. Lee, J. Phys. B **22**, 2705 (1989).
- [56] B. Lohmann, U. Hergenhahn, and N. M. Kabachnik, J. Phys. B **26**, 3327 (1993).
- [57] N. M. Kabachnik and I. P. Sazhina, J. Phys. B **35**, 3591 (2002).
- [58] E. G. Berezko and N. M. Kabachnik, J. Phys. B **11**, 2467 (1977).
- [59] K. N. Huang, Phys. Rev. A **26**, 2274 (1982).
- [60] I. P. Grant, in *Methods in Computational Chemistry*, edited by S. Wilson (Plenum Press, New York, 1988), Vol. 2, p. 1.
- [61] S. Fritzsche, Phys. Scr., T **T100**, 37 (2002).
- [62] F. A. Parpia, C. Froese Fischer, and I. P. Grant, Comput. Phys. Commun. **94**, 249 (1996).
- [63] S. Fritzsche, J. Electron Spectrosc. Relat. Phenom. **114–116**, 1155 (2001).
- [64] W. Ong and A. Russek, Phys. Rev. A **17**, 120 (1978).
- [65] B. Lohmann, J. Phys. B **32**, L643 (1999).
- [66] H. Klar, J. Phys. B **13**, 4741 (1980).